Spatial magnetic imaging of non-axially symmetric vortex domains in cylindrical nanowire by transmission X-ray microscopy

Fernandez Roldan, J. A.; Bran, C.; Asenjo, A.; Vázquez, M.; Sorrentino, A.; Ferrer, S.; Chubykalo-Fesenko, O.; Del Real, R. P.;

Originally published:

September 2022

Nanoscale 14(2022)37, 13661-13666

DOI: https://doi.org/10.1039/D2NR03228G

ARTICLE

Spatial magnetic imaging of non-axially symmetric vortex domains in cylindrical nanowire by Transmission X-ray Microscopy

Received 00th June 2022,
Accepted 00th June 2022

DOI: 10.1039/x0xx00000x

Jose A. Fernandez-Roldan[a]*, Cristina Bran[b], Agustina Asenjo[b], Manuel Vázquez[b], Andrea Sorrentino[c], Salvador Ferrer[c], Oksana Chubykalo-Fesenko[b] and Rafael P. del Real[b]*

The spatial magnetization texture of a cylindrical nanowire has been determined by Transmission X-ray Microscopy (TXM) and X-ray magnetic circular dichroism (XMCD). For this purpose, nanowires with designed geometry, consisting of CoNi/Ni periodic segments, have been grown by designed electrodeposition into alumina templates. Experimental data allows one to conclude the presence of mono- and trivortex magnetic domains in CoNi segments but, unusually, these states are characterized by an asymmetric XMCD contrast across the nanowire's section. Micromagnetic modelling shows non-trivial three-dimensional structures with ellipsoidal vortex cores and non-axially symmetric magnetization along the nanowire direction. The modelled TXM contrast of micromagnetic structures allows to correlate the experimental asymmetric XMCD contrast to the easy axis direction of the uniaxial magnetocrystalline anisotropy.

Introduction

The accumulated experience on nanoscale effects in planar nanostructures enables the take-off of 3D nanomagnetism that offers development of integrated devices based on 3D nanoarchitectures with curved geometries[1–3]. However, the experimental access to 3D morphologies is much more challenging than for planar systems and, so far, research to date has not yet explored all interesting complexities of the vast diversity of three-dimensional spin textures, with few exception[4,5]. In this scenario, magnetic cylindrical nanowires offer a controllable constant surface curvature and a wide range of potential capabilities from both fundamental and technological points of view[6-8]. The curvature and confinement of cylindrical nanowires (NW) promote novel non-trivial structures such as Bloch-point domain walls[9], helical magnetic configurations[10,11], vortices[12] or skyrmion tubes[13]. The identification of spin textures that could serve for novel technologies relies on the imaging of these diverse 3D magnetization textures in tailored nanowires. Magnetic tomography based on the Transmission X-ray Microscopy (TXM) and X-ray Magnetic Circular Dichroism (XMCD) imaging techniques has allowed the identification of buried magnetic textures such as 3D Bloch points as well as magnetic hophions[14–17]. The current challenge is to determine the magnetization spatial distribution in more complex 3D geometries[4,5,18,19]. For magnetic cylindrical nanowires, TXM-XMCD techniques are very promising for the access to detailed information of 3D magnetization configurations since this technique probes the full inner wire and not only its surface.

We aim at the deep understanding the 3D magnetization configuration in multisegmented CoNi/Ni cylindrical nanowires. The periodic change of the nanowire composition leads to an alternating magnetocrystalline anisotropy and domain structure in each segment[20–22]. Importantly, previous studies in CoNi nanowires report a large uniaxial magnetocrystalline anisotropy that promotes vortex domain structures[23], while Ni segments show a well-known axial magnetization. At the same time, the multisegmented nature with relatively small segment lengths, which we use in this article, ensures the presence of small number of magnetic domains in each segment due to the confinement effect.

Here, using TXM-XMCD imaging in combination with micromagnetic and TXM signal modelling, we have reconstructed the complex three-dimensional spin textures in the CoNi segments and determining the chirality and polarity of the vortex and showing how the direction of the magnetic easy axis influences on the shape and direction of the vortex structure in cylindrical nanowires.

Results and discussion

Multisegmented $[Co_{85}Ni_{15}/Ni]_{10}$ cylindrical nanowires were grown by controlled electrodeposition into alumina templates. Each NW consists of periodically alternating segments of CoNi alloy and Ni. NW diameter was about 140 nm and the average lengths were of approximately 1.2 and 1.0 µm for CoNi and Ni segments, respectively. The Ni segments present a face-centered cubic (fcc) structure while the CoNi segments show hexagonal close packed (hcp) CoNi crystalline structures.

[a] Helmholtz-Zentrum Dresden-Rossendorf e.V., Institute of Ion Beam Physics and Materials Research, 01328 Dresden, Germany.
[b] Instituto de Ciencia de Materiales de Madrid, CSIC. 28049 Madrid. Spain.
[c] ALBA Synchrotron. 08290 Cerdanyola del Vallés. Spain

Electronic Supplementary Information (ESI) available: The ESI includes additional information on micromagnetic simulations and the modelling of the TXM intensity profiles. The corresponding file is available free of charge: Supporting_Information.pdf (PDF file). See DOI: 10.1039/x0xx00000x

Further details on the synthesis, geometrical and structural characterization are reported elsewhere[24]. The sample was prepared for TXM through dilution of the template by chemical methods and deposition onto a SiN substrate.

Transmission X-ray microscopy

We performed the magnetic imaging of individual nanowires at the MISTRAL beamline of the ALBA Synchrotron light source. A full field transmission X-ray microscope that is equipped with monochromatic circularly polarized photons[23] permits the imaging of element specific magnetic contrast at the corresponding absorption energy in order to enhance the magnetic sensitivity of the X-ray absorption coefficient. Under resonant conditions, the magnetic dichroism depends on the dot product, δ $\boldsymbol{k}\cdot\boldsymbol{m}$, providing angular sensitivity to the absorption process in the direction of the X-ray wave vector k relative to the magnetization $\boldsymbol{m}$ (being δ the magnetic dichroism)[15]. The geometry of such experiment is illustrated in Figure 1(a). Here, the *y*-axis is normal to the SiN substrate (laying in the *xz*-plane) that supports the nanowires, and the x-axis is collinear with the nanowire axis; $\boldsymbol{k}$ (laying in the *xy* plane) is normal to the *z*-axis. In the experiment, the sample rotates by the angle α (within the *xy*-plane) around *z*-axis as indicated in Figure 1(a).

Prior to the imaging, we demagnetized the samples in a magnetic field perpendicular to the nanowire axis. We restrict our measurements within the incident range -45 º < α< 45 º and photon energies to the L3 (778.1 eV) and L2 (793.2 eV) absorption energies of Co to enhance the magnetic contrast since they have an opposite sign of the dichroism δ (which takes the values δ (L3) = 0.27 and δ (L2) = -0.20 [15,25]). As a result, the subtraction of two images suppresses the non-magnetic contribution while enhancing the magnetic contrast. At each incident X-ray direction, several images were acquired at the L3 and L2 photon energies, aligned and then subtracted. We estimated a ratio $\log(I_2)/\log(I_3) = 0.716$ between intensities at L2 and L3 edges. Finally, inhomogeneities in the illumination of the substrate by means of a normalization to a flat field image were corrected.

For easing the interpretation of our TXM results, we present in Figure 1(a-b) a perfect vortex configuration in the nanowire, for which the $\boldsymbol{k}\cdot\boldsymbol{m}$ product varies from positive to negative values across the NW section and therefore it produces a symmetric bright-dark contrast in TXM images. Figure 1(c) presents an experimental TXM image of the magnetic contrast in a part of a nanowire taken with normal incidence (α =0). The darkest and whitest spots at the interfaces between CoNi and Ni segments are ascribed to technical artifacts whose origin is still to be explained. Specifically, on this image we observe two CoNi segments showing magnetic contrast and, in between, an almost invisible segment which corresponds to Ni. The small contrast visible at the Ni segments arises from the slightly different charge absorption coefficient of Ni at the energies of Co L2 and L3 edges. The contrast obtained in Figure 1(c) qualitatively agrees with the results obtained in previous XMCD-PEEM measurements in similar nanostructures[24,26]. Here, the contrast in Figure 1(c) indicates a single vortex-like structure in the whole left CoNi segment, while the right segment (labelled trivortex) shows three vortices. Note that according to Figure 1 (b) the contrast sequence across the nanowire (dark-white or white-dark) is related with the vortex rotational sense (defined here as chirality[§]) and thus the central vortex in the trivortex evidences the same chirality as the single vortex in the left segment.

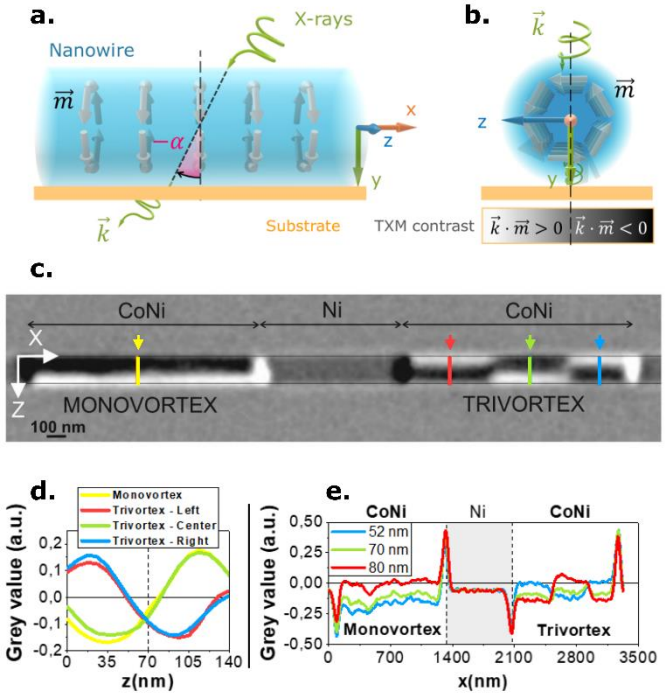

Figure 1. a) Description of the Transmission X-ray microscopy experiment. The X-ray beam with wave vector $\boldsymbol{k}$ is transmitted through the nanowire with an angle α with respect to the nanowire surface. The magnetization in the nanowire m adopts a perfect vortex configuration. b) Sketch for a purely symmetric vortex structure along the nanowire length; the sign of the dot product $\boldsymbol{k}\cdot\boldsymbol{m}$ switches exactly in the middle. c) TXM contrast for normal incidence (α =0) of a selected part of CoNi/Ni nanowire that show three segments: a CoNi Monovortex segment, Ni segment and a Trivortex CoNi segment. The profile of the contrast across the nanowire in the *z* direction at the four colored vertical lines is detailed in d): Monovortex, Trivortex-Left, Trivortex-Center and Trivortex-Right. The profile of the contrast along *x*-coordinate (along the nanowire) are represented in Figure e) at three different z values: 52 nm, 70 nm and 80 nm.

Most importantly, magnetic contrast is not symmetric with respect to the NW axis[22]. Figure 1(d) shows the magnetic contrast profile along the *z*-axis in the center of the vortices (marked by colored vertical lines in Figure 1(c)). The change of the contrast sign reflects different vortex rotational senses. Note that zero-contrast position is located at 52 nm for the vortices at the left and right sides of the trivortex state while it shifts to 80 nm for the monovortex and the central vortex in the trivortex state (called here trivortex-center). This is further

confirmed by the profile of the magnetic contrast along the nanowire for selected z values shown in Figure 1(e).
Another important result of Figure 1 is related to the transition between vortices with opposite chiralities in the trivortex state. While some theoretical studies have pointed out that the encounter of two vortices with opposite chirality produces a strongly topologically protected domain wall in nanowires[13,26], no experiments has directly imaged and confirmed its structure up to now.

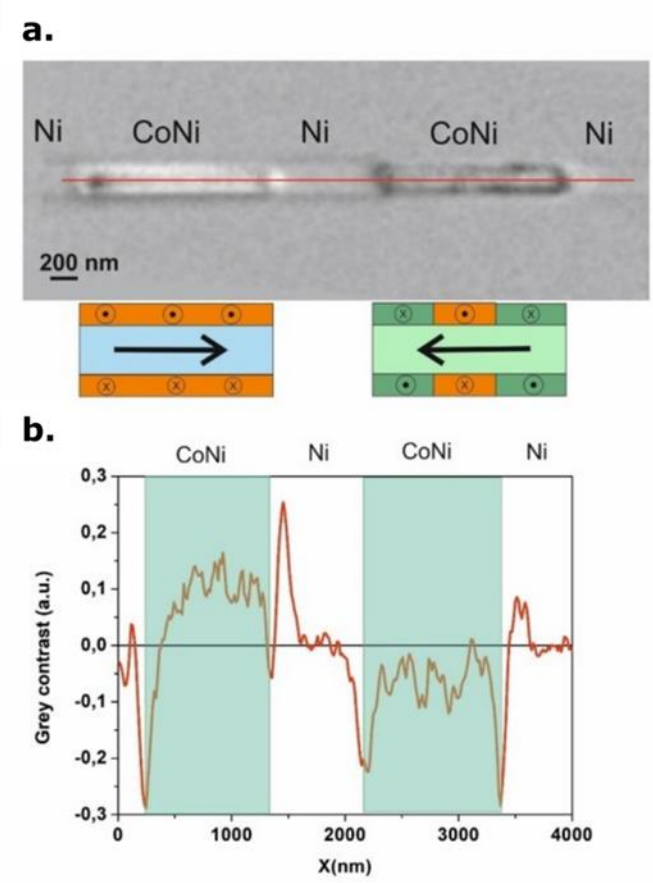

Figure 2. a) Top panel, magnetic contrast image obtained from the subtraction of images at ϑ=45º and ϑ =-45º, evidencing the axial magnetization direction. Bottom panel, a sketch illustrating the magnetic configuration (vortex chirality and polarity) for the CoNi segments with oversized cores. b) Profile of the magnetic contrast along the red horizontal line in a).

It is worth recalling that the addition of the contrast of the images for the same positive (α) and negative (-α) incident X-rays provides the magnetization in the y direction, while their subtraction mainly provides the magnetization along the nanowire (*x*-direction). Figure 2(a) presents the magnetic contrast proportional to the mx component of magnetization obtained from the images at the incidences α=±45º showing positive and negative axial magnetization orientations in the left and right segments, respectively. Figure 2(b) presents the value of the magnetic contrast along the red line that is marked in Figure 2(a). Here the positive and negative contrasts in the respective left and right CoNi segments confirm the rightwards and leftwards axial orientation of the magnetization in comparison with the vanishing contrast in Ni. Figure 2(a) (bottom panel) shows a schematic illustration of the polarity and chirality directions in each CoNi segment, based on the TXM contrasts introduced in Figures 1(c) and 2(a).

Micromagnetic modelling of spin textures and vortex domains

In order to unveil the magnetic configurations leading to the asymmetric contrast that is depicted in Figure 1(c), we have performed micromagnetic modeling of the corresponding magnetic states that will later be used to evaluate their theoretical TXM contrast. Specifically, we modelled the monovortex and trivortex magnetic states in a bisegmented CoNi/Ni nanowire with periodic boundary conditions using the mumax3 micromagnetic code[27] (See section 1 in Electronic Supplementary information). Co rich nanowires typically grow with hexagonal crystal structure whose c axis is nearly perpendicular to the nanowire axis[28], as is our case. Thus, the hcp crystal structure gives rise to a high magnetocrystalline anisotropy and in competition with the shape anisotropy it promotes the formation of magnetic vortex states[28,29].

Nevertheless, the magneto-crystalline easy axis direction may also slowly vary along the same nanowire due to the presence of dislocations. Because of this fact, in our modelling we performed a systematic study, varying the value and orientation of the magneto-crystalline anisotropy axis inside CoNi segments (See section 1.1 in ESI). Two representative examples of the modelled monovortex state in a CoNi segment for two orientations of the easy axis magnetization directions ϑ with respect to the nanowire axis are presented in Figure 3(a-b). The left panels of these figures show a cross section of the magnetization profile in a vortex magnetic domain colored according to axial component of the magnetization m_x. For ϑ=88º the isolines and the profiles of m_x component along *y*- and *z*-axis demonstrate the ellipse-like shape of the asymmetric vortex core with a long axis parallel to the easy axis of the magnetocrystalline anisotropy (*y*-direction), which is almost perpendicular to the nanowire. The measurement of the half width at medium height gives core sizes of 68 and 22 nm along long and short elliptical axes, respectively. Significantly, the core center is located on the nanowire axis in the middle of the segment, although it deviates slightly from the nanowire axis in the vicinity of the CoNi/Ni interfaces. Our studies also confirm that the core elongation depends on the value of the anisotropy constant (see section 1.1 in ESI).

Turning now to the magnetic state in the CoNi segment with the anisotropy axis forming ϑ=60º with the nanowire axis (Figure 3(b)), we observe more revealing results. Here, the magnetization profile in the NW cross-section shows a very asymmetric structure along *z*-direction (the upper red and the bottom blue colors stand for m_x>0 and m_x<0) in contrast to the vanishing magnetization of the vortex state in Figure 3(a)(left). While a naïve view in terms of colors may resemble two magnetic domains, the isolines point the area with largest m_x>0

and confirm a complex three-dimensional vortex-like structure with a large distortion of the ellipsoidal-like core shape. Our studies of the magnetization on the surface of the nanowire (more details in ESI section 1.2) suggest that the plane containing the vortex has rotated by some angle in the direction of the easy axis.

Figure 3. Micromagnetic configurations of monovortex (a-b) and

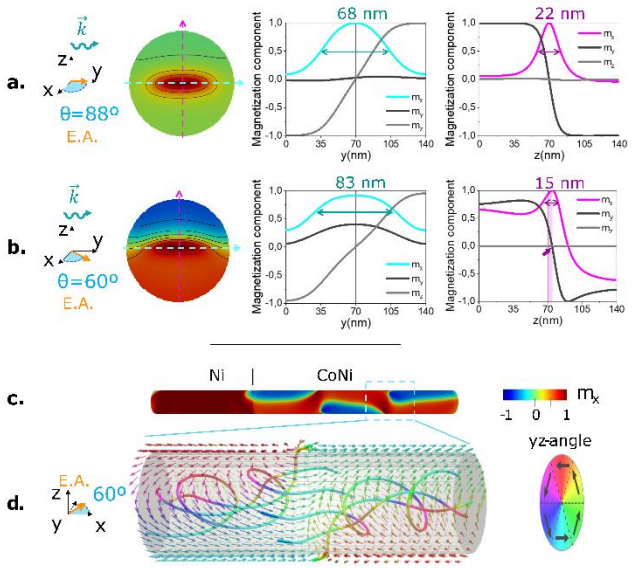

trivortex (c-d) states in CoNi segments: (a-b) Left- m_x axial magnetization component in the cross section of the simulated CoNi monovortex at x=600 nm (the center of the monovortex) for (a) ϑ=88º and (b) ϑ=60º respectively. The easy axis direction is assumed to lay in the xy plane. Right: Vortex profile (m_x, m_y and m_z) of the elliptical vortex along y- and z-axis (c) Axial magnetization component in simulated trivortex state with and ϑ=60º. (d) Selected magnetization streamlines in the region delimited in (c), showing the vortex core displacement inside the nanowire. Arrows on the surface indicates the direction of the magnetization on the surface. Coloring of arrows and streamlines indicates the magnetisation yz-angle.

The profiles of the m_x and m_y magnetization components in Figure 3(b) (center-right), symmetric with respect to the y-axis, allows to estimate the vortex core size of 83 nm along this direction, much larger than for ϑ =88º. Definition of the core size corresponding to the decrease of the magnetization value in two times from its maximum in both sides for the m_x component along z-direction, provides a width around 16 nm, smaller than for the ϑ=88º case. Additionally, there is a small displacement of the vortex core center (defined where m_x is maximum) of 5 nm along the z axis. Most importantly, a larger tilt of the easy axis of the magnetic anisotropy towards the nanowire axis induces a longitudinal magnetization component (m_x) which takes either positive or negative values at the nanowire surface, breaking the axial symmetry of the magnetization profile. This lack of circular symmetry of the magnetization configuration is responsible for the asymmetric TXM contrast, as we will prove below.

For the trivortex state modelled for ϑ=60º (see the magnetization configuration on the nanowire surface in Figure 3(c)), the profiles of the vortices in the domain center are similar to that of the monovortex state. However, the encounter between two vortex domains with opposite chirality leads to a strongly topologically protected three-dimensional domain wall, which here is represented by the streamlines. In this domain wall the vortex cores (helical streamlines) repel each other in the opposite direction, towards the nanowire surface (see Figure 3(d)). In the wall center, the vortex cores exit on the nanowire surface forming two surface vortices with the chirality of the inner vortices. Further analysis (details in section 1.2 of the ESI) confirms that for each vortex, a corresponding anti-vortex with the same polarity is formed on the surface, so that the domain wall consists of two surface vortices and two anti-vortices. Thus, modelling indicates that the darker areas in the right segment in the TXM contrast in Figure 2(a) could be ascribed to this three-dimensional domain wall.

Modelling Transmission X-ray contrast from micromagnetic spin textures.

With the aim to identify the TXM contrast in the experiment, we have evaluated the X-ray transmission intensities from the micromagnetic states in conditions close to the experiment. The intensity of the transmitted signal $I_L(x,y,z)$ depends on the normalized magnetization $\boldsymbol{m}(x,y,z)$ defined by the equations:

$$\frac{\partial}{\partial y}\ln I_{L3}(\alpha) = -\frac{0.85}{AL(L3)\cos(\alpha)}\,(1+\delta(L3)\,\boldsymbol{k}(\alpha)\cdot\boldsymbol{m}), \quad (1)$$

$$\frac{\partial}{\partial y}\ln I_{L2}(\alpha) = -\frac{0.85}{AL(L2)\cos(\alpha)}\,(1+\delta(L2)\,\boldsymbol{k}(\alpha)\cdot\boldsymbol{m}), \quad (2)$$

where the coefficient 0.85 accounts for the 85% Co composition of the segment. The absorption of Ni is neglected since it is much smaller than that of Co. AL(L3) and AL(L2) are the X-ray absorption lengths of Co at the L3 and L2 energies, respectively. The magnitudes of AL(L3) and AL(L2) were experimentally determined by measuring transmission spectra of an ensemble of clustered nanowires. The obtained values, AL(L3) = 82.8 nm and AL(L2) = 102.7 nm, include the different transmissions of the beamline monochromator and optics at the two photon energies.

Our modelling confirms that the contrast asymmetry can be only explained if we assume that the easy axis of magnetic anisotropy forms a certain angle ϑ <90º, with the nanowire axis (more details in section 2 of ESI). In this case the contrast depends also on the position of the nanowire on the substrate, since the nanowire can be rotated around its axis, which is translated to a different angle between the X-ray incidence direction and the magnetocrystalline easy axis, φ. Note that a rotation of the easy axis around the nanowire axis switches the contrast in the monovortex state as well as the domain wall orientation, whose internal structure is oriented parallel to the easy axis of anisotropy (See section 2.2 in ESI).

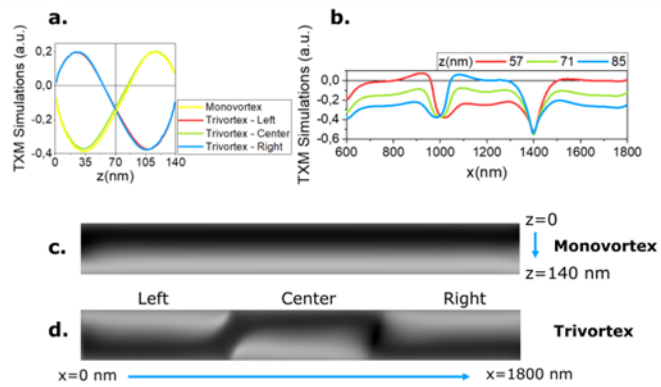

Figure 4. (a) Profiles of the modelled magnetic contrasts evaluated across (c) monovortex and (d) trivortex simulated TXM images. (b) Profiles of the modelled contrast along the *x*-direction for 3 different z values of the trivortex simulated TXM image: *z*=57 nm, 71 nm and 85 nm. The results were extracted from simulations with the easy axis in CoNi segments forming ϑ =60º with the nanowire axis and ϕ=225º with respect to the y axis.

The extensive study allowed us to fit the TXM contrast and magnetic configuration closer to the experiment in a CoNi segment with anisotropy easy axis at ϑ=60º and ϕ= 225º with respect to the y axis. Figure 4(c-d) stands for the simulated magnetic contrast for the monovortex and trivortex states. The profiles of the simulated contrast in the *z*-direction of the monovortex and trivortex in Figure 4 (a-b) show the asymmetric magnetic contrast across the nanowire axis, similar to that of Figure 1(d). Additionally, the simulated image shows the same directions of 3D domain walls, separating domains with opposite chiralities, in agreement with the experiment shown in Figure 1(c). Furthermore, similar to the experimental profiles in Figure 1(e), the simulated contrast in Figure 4(b) along x-direction in the trivortex segment (for *z* =57, 71 and 85 nm) evidences that the magnetic contrast displaces to more negative values with the increase of the *z* coordinate in the left and right vortices and to positive values for the central vortex. Additionally, for *z*=71 nm the contrast is always negative in agreement with the experiment. Thus, the agreement between modelling and experiment defines a unique position of the crystalline easy axis with respect to nanowire and X-ray propagation directions.

It is also worth noticing the different simulated TXM contrast shown by the two DWs in Figure 4(b). This difference has been also observed experimentally (Figure 1(c) and 1(e)) and it is explained due to a 90º rotation of the right DW with respect to the left one as it is made evident in the simulated micromagnetic configuration shown in Figure 3(c).

Conclusions

In summary, the magnetic transmission X-ray microscopy with an accurate magnetic contrast analysis has allowed us a precise determination of the chirality and polarity of the mono and trivortex structures in CoNi segments in CoNi/Ni multisegmented cylindrical nanowires. The observed TXM contrast appeared to be asymmetric in the transverse direction. Micromagnetic simulations suggest that the shift of the contrast is introduced by complex non-axially symmetric vortex structures produced by a competition between shape and magnetocrystalline anisotropy which easy axis forms an angle of ca. 60º with the nanowire axis. Its orientation with respect to the X-ray propagation direction has been also uniquely identified. Importantly, vortex cores have ellipsoidal shapes. The transition between the trivortex domains with opposite chirality is given by a new three-dimensional domain wall that is strongly topologically protected. Inside this wall vortex cores repel each other and exit to nanowire surface. Our results open new perspectives for the investigation of new types of challenging complex three-dimensional magnetic states for information technology applications.

Author Contributions

We strongly encourage authors to include author contributions and recommend using CRediT for standardised contribution descriptions. Please refer to our general author guidelines for more information about authorship.

Conflicts of interest

There are no conflicts to declare.

Acknowledgements

This work was supported by the Spanish Ministry of Innovation and Science under project PID2019-108075RB-C31/AEI/10.13039/501100011033, and the Regional Government of Madrid under project P2018/NMT-4321 NANOMAGCOST. These experiments were performed at MISTRAL beamline at ALBA Synchrotron with the collaboration of ALBA staff. Jose A. acknowledges the support provided by the Alexander von Humboldt Foundation.

Notes and references

§ Note That from the Geometrical Point of View Chirality Should Be Defined as a Product of Rotational Sense (Vorticity) and Polarity. Here We Follow a Definition Accustomed in the Theory of Magnetic Vortices Where Chirality Is Defined as the Rotational Sense Only.

1 A. Fernández-Pacheco, R. Streubel, O. Fruchart, R. Hertel, P. Fischer and R. P. Cowburn, *Nature Communications*, 2017, **8**, 15756.
2 R. Streubel, P. Fischer, F. Kronast, V. P. Kravchuk, D. D. Sheka, Y. Gaididei, O. G. Schmidt and D. Makarov, *Journal of Physics D: Applied Physics*, 2016, **49**, 363001.
3 D. D. Sheka, *Applied Physics Letters*, 2021, **118**, 230502.
4 C. Donnelly, A. Hierro-Rodríguez, C. Abert, K. Witte, L. Skoric, D. Sanz-Hernández, S. Finizio, F. Meng, S. McVitie, J. Raabe, D. Suess, R. Cowburn and A. Fernández-Pacheco, *Nature Nanotechnology 2021*, 2021, 1–7.

5 S. Gliga, G. Seniutinas, A. Weber and C. David, *Materials Today*, 2019, **26**, 100–101.
6 M. Vázquez, Magnetic Nano- and Microwires: Design, Synthesis, Properties and Applications, Elsevier, 2020.
7 C. Bran, J. A. Fernandez-Roldan, R. P. del Real, A. Asenjo, O. Chubykalo-Fesenko and M. Vazquez, *Nanomaterials 2021, Vol. 11, Page 600*, 2021, **11**, 600.
8 Jeon, Y. S., Shin, H. M., Kim, Y. J., Nam, D. Y., Park, B. C., Yoo, E., Kim, H. R.; Kim, Y. K. *ACS Applied Materials and Interfaces*, 2019, **11**, 23901–23908. DOI:10.1021/ACSAMI.9B06535
9 S. da Col, S. Jamet, N. Rougemaille, A. Locatelli, T. O. Mentes, B. S. Burgos, R. Afid, M. Darques, L. Cagnon, J. C. Toussaint and O. Fruchart, *Physical Review B*, 2014, **89**, 180405.
10 A. S. Arrott, *IEEE Magnetics Letters*, 2016, **7**, 1–5.
11 Y. P. Ivanov, A. Chuvilin, L. G. Vivas, J. Kosel, O. Chubykalo-Fesenko and M. Vázquez, *Scientific Reports*, 2016, **6**, 23844.
12 Y. P. Ivanov, M. Vázquez and O. Chubykalo-Fesenko, *Journal of Physics D: Applied Physics*, 2013, **46**, 485001.
13 J. A. Fernandez-Roldan, R. Perez del Real, C. Bran, M. Vazquez and O. Chubykalo-Fesenko, *Nanoscale*, 2018, **10**, 5923–5927.
14 A. Hierro-Rodriguez, D. Gürsoy, C. Phatak, C. Quirós, A. Sorrentino, L. M. Álvarez-Prado, M. Vélez, J. I. Martín, J. M. Alameda, E. Pereiro and S. Ferrer, *Journal of Synchrotron Radiation*, 2018, **25**, 1144–1152.
15 C. Blanco-Roldán, C. Quirós, A. Sorrentino, A. Hierro-Rodríguez, L. M. Álvarez-Prado, R. Valcárcel, M. Duch, N. Torras, J. Esteve, J. I. Martín, M. Vélez, J. M. Alameda, E. Pereiro and S. Ferrer, *Nature Communications*, 2015, **6**, 8196.
16 A. Hierro-Rodriguez, C. Quirós, A. Sorrentino, L. M. Alvarez-Prado, J. I. Martín, J. M. Alameda, S. McVitie, E. Pereiro, M. Vélez and S. Ferrer, *Nature Communications 2020 11:1*, 2020, **11**, 1–8.
17 N. Kent, N. Reynolds, D. Raftrey, I. T. G. Campbell, S. Virasawmy, S. Dhuey, R. v. Chopdekar, A. Hierro-Rodriguez, A. Sorrentino, E. Pereiro, S. Ferrer, F. Hellman, P. Sutcliffe and P. Fischer, *Nature Communications 2021 12:1*, 2021, **12**, 1–7.
18 C. Donnelly, M. Guizar-Sicairos, V. Scagnoli, S. Gliga, M. Holler, J. Raabe and L. J. Heyderman, *Nature*, 2017, **547**, 328–331.
19 D. Sanz-Hernández, A. Hierro-Rodriguez, C. Donnelly, J. Pablo-Navarro, A. Sorrentino, E. Pereiro, C. Magén, S. McVitie, J. M. de Teresa, S. Ferrer, P. Fischer and A. Fernández-Pacheco, *ACS Nano*, 2020, **14**, 8084–8092.
20 M. Méndez, S. González, V. Vega, J. Teixeira, B. Hernando, C. Luna and V. Prida, *Crystals (Basel)*, 2017, **7**, 66.
21 V. M. Prida, J. García, L. Iglesias, V. Vega, D. Görlitz, K. Nielsch, E. Barriga-Castro, R. Mendoza-Reséndez, A. Ponce and C. Luna, *Nanoscale Research Letters*, 2013, **8**, 263.
22 E. Berganza, M. Jaafar, C. Bran, J. A. Fernández-Roldán, O. Chubykalo-Fesenko, M. Vázquez and A. Asenjo, *Scientific Reports*, , DOI:10.1038/s41598-017-11902-w.
23 C. Bran, J. A. Fernandez-Roldan, R. P. Del Real, A. Asenjo, Y.-S. Chen, J. Zhang, X. Zhang, A. Fraile Rodríguez, M. Foerster, L. Aballe, O. Chubykalo-Fesenko and M. Vazquez, *ACS Nano*, 2020, **14**, 12819–12827.
24 C. Bran, J. A. Fernandez-Roldan, E. M. Palmero, E. Berganza, J. Guzman, R. P. del Real, A. Asenjo, A. Fraile Rodríguez, M. Foerster, L. Aballe, O. Chubykalo-Fesenko and M. Vazquez, *Physical Review B*, 2017, **96**, 125415.
25 C. T. Chen, Y. U. Idzerda, H.-J. Lin, N. V. Smith, G. Meigs, E. Chaban, G. H. Ho, E. Pellegrin, and F. Sette. *Physical Review Letters*, 1995, **75**, 152–155. DOI: 10.1103/PhysRevLett.75.152
26 S. Ruiz-Gómez, M. Foerster, L. Aballe, M. P. Proenca, I. Lucas, J. L. Prieto, A. Mascaraque, J. de la Figuera, A. Quesada and L. Pérez, *Scientific Reports 2018 8:1*, 2018, **8**, 1–6.
27 A. Vansteenkiste, J. Leliaert, M. Dvornik, M. Helsen, F. Garcia-Sanchez and B. van Waeyenberge, *AIP Advances*, 2014, **4**, 107133.
28 27 Y. P. Ivanov, D. G. Trabada, A. Chuvilin, J. Kosel, O. Chubykalo-Fesenko and M. Vázquez, *Nanotechnology*, 2014, **25**, 475702.
29 28 Z. Liu, P. C. Chang, C. C. Chang, E. Galaktionov, G. Bergmann and J. G. Lu, *Advanced Functional Materials*, 2008, **18**, 1573–1578.

